P.F. Barbante, A. Frezzotti
A Comparison of Models for the Evaporation of the Lennard-Jones Fluid
European Journal of Mechanics B. Fluids, Vol. 64, 2017, p. 69-80
doi:10.1016/j.euromechflu.2017.01.020

A comparison of models for the evaporation of the Lennard-Jones fluid

Paolo Barbante

Politecnico di Milano, Dipartimento di Matematica, Via E. Bonardi 9 - 20133 Milano - Italy

Aldo Frezzotti

Politecnico di Milano, Dipartimento di Scienze e Tecnologie Aerospaziali, Via La Masa 34 - 20156 Milano - Italy

---

Abstract

The evaporation of a thin liquid film is studied by a diffuse interface model whose thermodynamic and transport properties are consistent with those of the Lennard-Jones fluid. Solutions are obtained for various liquid film temperatures and downstream vapor flow velocities. The results are compared with reference molecular dynamics simulations of a system of atoms interacting by the $6-12$ Lenard-Jones potential. It is shown that the diffuse interface model underestimates the temperature drop across the non-equilibrium vapor region next to the liquid-vapor interface but overestimates the density drop, thus predicting smaller evaporation rates. Results indicates that the discrepancies between molecular dynamics and diffuse interface model predictions become smaller when the liquid film temperature approaches the critical temperature and the vapor becomes a dense, non-ideal gas. Further successful comparisons of molecular dynamics results with the predictions of a hybrid model, combining the continuum description of the liquid with the kinetic description of the vapor, suggest that the observed discrepancies can be attributed to poor description of the Knudsen layer provided by the diffuse interface model when the vapor phase is dilute.

Keywords: Evaporation, diffuse interface models, molecular dynamics, hybrid models

2010 MSC: 76T10, 82C24, 76P05, 82C80

1. Introduction

Diffuse interface models (DIMs) provide an interesting and rapidly developing approach to the study of multiphase flows [1, 2]. In the case of a fluid with coexisting liquid and vapor regions, DIMs are capable of a unified description of both phase bulks and interfacial regions, thanks to the presence of an additional contribution in the static part of the stress tensor, which is made to depend on the spatial derivatives of the density field [1, 2], following Korteweg theory of capillary phenomena [3]. Non-equilibrium effects are taken into account by adding viscous stresses, in the classical form of Navier-Stokes constitutive law, to static ones. Similarly, the fluid internal energy and Fourier law expression for heat flux are modified by terms depending on density gradients [1, 2]. In principle, DIMs treatment of multiphase flows offers several advantages. A single mathematical model, based on a small number of PDEs, describes the liquid, vapor and interface regions. Any need to adopt boundary conditions at vapor-liquid interface to take into account evaporation/condensation phenomena [4, 5] is eliminated. Moreover, no interface tracking technique is necessary in DIMs based numerical simulations, since the finite thickness interfacial regions are part of the flowfield. Such attractive features have been exploited to study liquid jets instabilities, spinodal decomposition, boiling and bubble dynamics [6, 7, 8]. DIMs studies, specifically addressing evaporation/condensation flows, are scant and limited to qualitative analysis of flow properties [9, 10].
Although attractive, DIMs description of evaporation or condensation phenomena is not automatically accurate. As a matter of fact, when the vapor phase is dilute a kinetic layer (Knudsen layer) [11, 12] is always formed in the vicinity of the vapor-liquid interface, during evaporation or condensation. This kinetic region extends into the vapor for a few mean paths, depending on the intensity of the mass flow rate. Macroscopic flow properties suffer rapid changes which are not well described by hydrodynamic equations. Since DIMs adopts

Navier-Stokes and Fourier constitutive laws, some deviations from the correct fluid behavior are to be expected. The present work aims at extending a preliminary investigation about the accuracy of DIMs in describing evaporation flows [13]. The evaporation of a planar liquid film is used as test problem. Accurate Molecular Dynamics (MD) simulations of the Lennard-Jones fluid are performed to obtain the benchmark flowfield structure in the liquid, vapor and interface regions, without any additional assumption beyond those intrinsic in the classical MD simulation of fluids.

In conducting the comparison of MD computed flow properties with DIMs results, particular care has been taken in constructing a diffuse interface model matching the thermodynamic [14] and transport properties [15, 16] of the Lennard-Jones fluid. In order to highlight the role of kinetic effects in the Knudsen layer, MD and DIM results are also compared with computations based on a hybrid model (HM) in which the liquid region is described by hydrodynamic equations, whereas the vapor is governed by the Boltzmann equation [17]. The liquid and vapor phase are separated by a structureless interface, replaced by kinetic boundary conditions [4]. According with the above considerations, the paper content is organized as follows: Section 2 describes the test problem characteristics; MD simulations are described in Section 3, whereas DIM structure, its numerical implementation and results are described in Section 4. The kinetic model structure and numerics are described in Section 5, along with results and comparisons with the reference MD calculations.

2. Test problem description

A simple test problem is used to assess the capabilities of DIM and HM in describing the evaporation of a simple Lennard-Jones liquid. A liquid film, in the form of an infinite planar slab of finite thickness Δz_l, is initially in equilibrium with its vapor phase at temperature T_l. The vapor occupies two regions, symmetrically located with respect to the liquid slab center. Each of them is delimited by the adjacent liquid-vapor interface and an impermeable and adia-

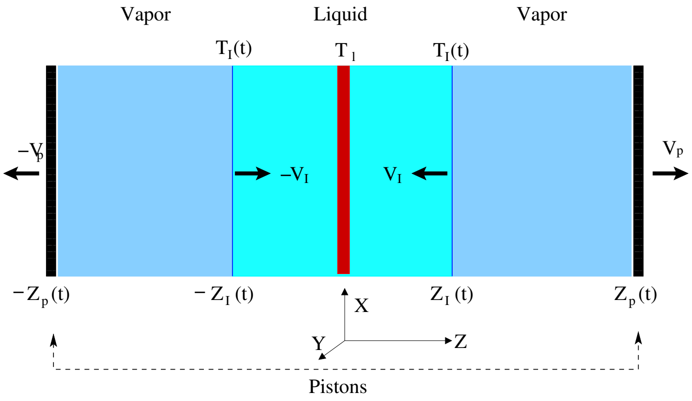

Figure 1: Sketch of test problem set up.

batic piston, whose planar surface is kept parallel to the vapor-liquid interface. The left and right pistons are initially located in the vicinity of the vapor-liquid interface at positions $-z_p(0)$ and $z_p(0)$, respectively. Evaporation flow is then started by withdrawing both pistons with constant opposite speeds $\mp v_p$. During evaporation, the center of the liquid slab is kept at constant temperature T_l to avoid excessive cooling of the liquid slab. The resulting flow is unsteady, because of the interfacial motion and the time evolution of the non-uniform temperature profile in the liquid. However, the receding interfaces common temperature $T_I(t)$, after an initial rapid transient cooling, reaches a minimum followed by a slow monotonic increase. If the initial slab thickness is large enough, the part of the $T_I(t)$ curve following the minimum is so slowly increasing to be considered a constant plateau. In this phase of the system evolution, the temperature profile in the liquid takes an approximately linear shape evolving self-similarly. If the duration of the temperature plateau is long enough with respect to the time sound waves in the vapor take to travel through the gap between the piston and the interface, then the vapor flow becomes quasi-steady. Its structure is relatively simple, consisting in a kinetic region (Knudsen layer) next to the interface, followed by a uniform equilibrium region where the vapor moves with the piston speed. Vapor density and temperature are dictated by the proper kinetic jump relationships [4, 11, 12, 18], determined by the microscopic mech-

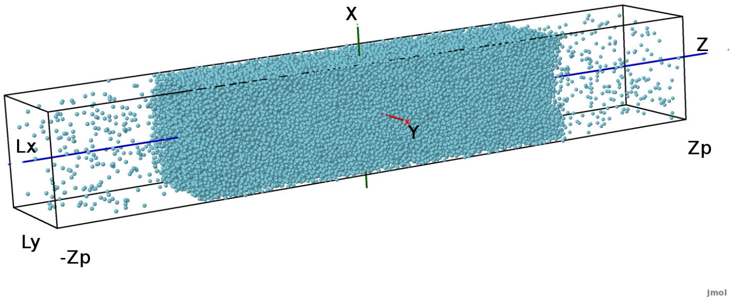

Figure 2: Scheme of Molecular Dynamics simulation domain geometry.

anisms governing molecular emission from the liquid phase into the vapor and vapor molecules scattering from the liquid surface [19, 20, 5]. Hence, the present test problem represents a good probe of the capabilities of a model to reproduce transport properties at the vapor-liquid interface.

3. Molecular dynamics simulations of a liquid film evaporation

The role of molecular dynamics (MD) [21] simulations is to provide the most fundamental description of the test problem and the reference flowfield properties. It is assumed that the fluid is composed by N_a identical atoms of mass m, interacting pairwise through forces derived from the following Lennard-Jones (LJ) $6-12$ potential $\phi_{LJ}(r)$ [22]:

$$\phi_{LJ}(r) = 4\epsilon \left[\left(\frac{\sigma}{r} \right)^{12} - \left(\frac{\sigma}{r} \right)^{6} \right] \tag{1}$$

In Eq. (1), r the distance between two interacting atoms, ϵ is the depth of the potential well, whereas the length σ defines the effective range of atomic forces. More precisely, $r_m = 2^{1/6}\sigma$ is the position of the potential minimum.

The atomic mass and the LJ potential parameters have been adopted as natural units for all fluid properties defined in the paper. Accordingly, length, time and mass are normalized with respect to the natural space, time and mass scales of atomistic simulations, namely σ, $\sqrt{\frac{m\sigma^2}{\epsilon}}$ and m, respectively. Temperature is normalized to $\frac{\epsilon}{k_B}$, being k_B the Boltzmann constant. Throughout the paper, the symbol ρ is associated with the fluid reduced density $n\sigma^3$, being n the fluid number density. The described normalizations has been also used in the Diffuse Interface Model and in the hybrid continuum-kinetic model described below.

Atomic motions are computed numerically by integrating Newton's equations by the velocity Verlet scheme [21]. The time step, in LJ units, has been varied between $2.0e-03$ and $5.0e-03$. The infinite system is constructed as the union of periodic replicas of the finite fluid column sketched in Figure 2. The MD computational domain has fixed side lengths L_x and L_y along the two directions x and y, where periodic boundary conditions [21] are applied, being parallel to the liquid surface. Along the direction normal to the liquid surface, spanned by the coordinate z, the column height is delimited by the piston positions. Forces have been computed according to the minimum image convention [21], after truncating atomic interactions of pairs whose relative distance r exceeds a specified cut-off radius r_c. The latter been set equal to 3.0σ to keep the computational time within reasonable limits. A spatial grid, with a cell size of r_c, has been used to index atoms and make the search of nearest neighbors more efficient. Although intrinsically three-dimensional, the adopted MD setup guarantees that *ensemble* averaged macroscopic quantities will depend only on z and t, thus approximating the infinite system described in Section 2 in a statistical sense.

Each computation has been started from an initial state in which a liquid slab, located in the center of the computational box, is in equilibrium with its vapor at a specified temperature T_l. The vapor occupies the two symmetrical gaps located between the vapor-liquid interfaces and the box walls at $z = \mp z_p(t)$, consisting of two specularly reflecting pistons which, at time $t = 0$, are impulsively set into motion with opposite constant velocities $\mp v_p$, in order to increase the vapor gaps volume and cause liquid evaporation. The simulation box lengths L_x and L_y have been set equal to $8r_c$, or 24σ. The initial values of the liquid slab thickness has been set equal to 80σ for the simulations with lower evaporation rates ($T_l = 0.80, 0.85, 0.90$, $v_p = 0.10, 0.15$) and increased to 90σ when the either

$T_l > 0.90$ or $v_p = 0.2$. In the case $T_l = 1.05, v_p = 0.2$ the initial slab thickness has been set equal to 100σ. The described system initialization ensures a sufficiently long temperature plateau duration after the transient liquid surface cooling. Depending on the T_l and the initial slab thickness, N_a varied from about 3.3×10^4 to about 4.0×10^4. During the evaporation process, a narrow central strip of the liquid slab, $3.0 - 4.0\sigma$ wide, is thermostatted at temperature T_l by a simple Gaussian thermostat [21]. Local values of the fluid macroscopic quantities have been obtained by sampling microscopic states of atoms belonging to the same spatial cell. The cell system for macroscopic quantities estimation is not the same used for atom indexing, having a resolution of a small fraction of σ (typically $\sigma/4$). The time evolution of the system macroscopic properties has been obtained by dividing the total simulation duration into a number of time windows and computing time averaged system properties in each window. The amplitude of the time window is small enough to make the interface motion have a negligible effect on sampling spatial profiles. To further increase the number of microscopic samples in the vapor phase, each time averaged profile has been obtained by superposing the results of 48 statistically independent parallel simulations of the (macroscopically) same system, each one using N_a atoms. The system sizes, in terms of spatial extensions and simulated atoms number, are believed to be adequate in view of the comparison with DIM described below. Actually, the column widths L_x, L_y, the liquid slab half-thickness and N_a are definitely larger than the corresponding values used in MD simulations aimed at deriving the LJ fluid transport properties used in DIM (see Ref. [15] and references therein). Moreover, the comparisons described in the present paper show the same degree of deviation from DIM and HM found in a preliminary study of the same test problem [13], where *smaller* systems have been used.

Owing to the high number of atoms in the liquid phase and the relatively large number of independent samples (48) used in ensemble averages, the liquid phase profiles, as well as the interface motion and temperature show run to run variations well below 1%. In the vapor phase, samples size is smaller and variance higher, as can be seen from the profiles displayed in Fig. 5. The

T	ρ_l	ρ_v	l_v	$Z = p/\rho_v T$
0.80	0.761	$1.226e-02$	11.46	0.914
0.85	0.734	$1.887e-02$	6.874	0.882
0.90	0.706	$2.793e-02$	4.785	0.844
0.95	0.675	$4.023e-02$	3.416	0.799
1.00	0.641	$5.705e-02$	2.473	0.744
1.05	0.600	$8.091e-02$	1.745	0.676

Table 1: Test simulations equilibrium properties values in LJ units. ρ_l and ρ_v are the liquid and vapor reduced densities, respectively.

relative error associated with the MD estimations of macroscopic quantities in the gas phase is in the range $1.0 - 1.5\%$. MD results reported here have been obtained for the values of the liquid temperature listed in Table 1. Three piston speed values have been considered: $v_p = 0.10, 0.15, 0.20$. Such velocity settings produce downstream flow Mach numbers of the same order of magnitude and Knudsen layers of thickness of the order of $1.0 - 3.0$ mean free paths, equivalent to several atomic diameters σ. Table 1 also summarizes the equilibrium properties of the liquid and vapor at the temperatures specified above. In particular, the rightmost two columns contain the values of vapor mean free path l_v and compressibility $Z = P_v/(R\rho_v T_l)$, being P_v the vapor pressure, ρ_v the vapor density and $R = k_B/m$ the gas constant. The Lennard-Jones fluid pressure has been computed from the equation of state proposed in Ref. [14] in the form:

$$P = \rho T + \sum_{i=1}^{8} a_i(T)\rho^{(i+1)} + \exp\left(-3\rho^2\right)\left[\sum_{i=1}^{6} b_i(T)\rho^{(2i+1)}\right] \tag{2}$$

In Eq. (2), all quantities are expressed in the Lennard-Jones units mentioned above. The coefficients $a_i(T)$ and $b_i(T)$ are rational functions of the temperature T, defined by 32 parameters whose values have been determined by MD simulations [14]. It should be noted that mean free path value has only an indicative meaning. As a matter of fact, it has been evaluated from the gas shear

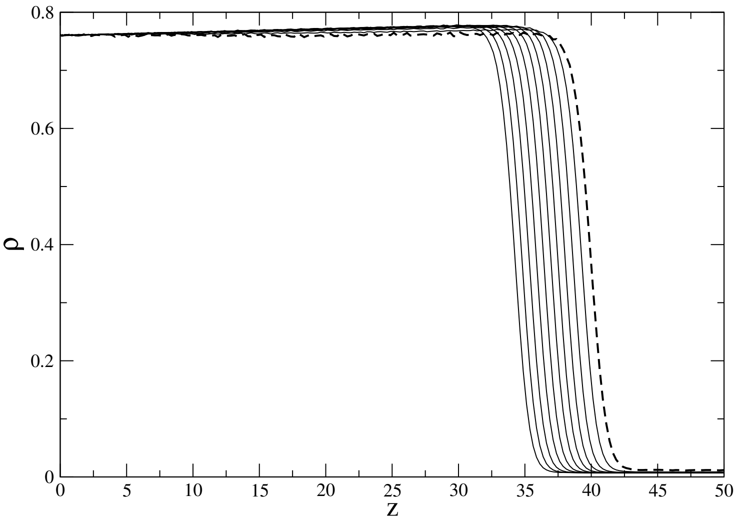

Figure 3: MD computed time evolution of density profile; $T_l = 0.80$, $v_p = 0.15$. Dashed line: initial density profile. Density profiles displayed every 200 time units.

viscosity μ, following the dilute gas expression for hard sphere interaction [23]:

$$l_v = \frac{16\mu}{5\sqrt{2\pi R T_l}\rho_v} \tag{3}$$

although the vapor conditions are close to ideal ones only for the lowest temperature values. The viscosity of the LJ fluid has been computed by the expression given in Ref. [15] which, in the limit $\rho \to 0$, reduces to the ideal LJ gas viscosity in the form:

$$\mu^{(id)}(T) = \frac{5}{16\sqrt{\pi}} \frac{\sqrt{T}}{\Omega^{(2,2)}(T)} \tag{4}$$

where the transport collision integral $\Omega^{(2,2)}(T)$ [23] has been approximated as described in Ref. [24].

The results of a typical MD simulations of the evaporation of a planar liquid film are reported in Figures 3, 4 and 5. Figure 3 shows the time evolution of the density profile when the temperature T_l is set equal to 0.8 and the piston speed v_p is equal to 0.15. Density profiles are displayed at equally spaced time intervals of 200 time units $t = \sigma\sqrt{\frac{m}{\epsilon}}$. The profile evolution shows that, after a short transient, the interface density profile recedes while keeping the same shape. In

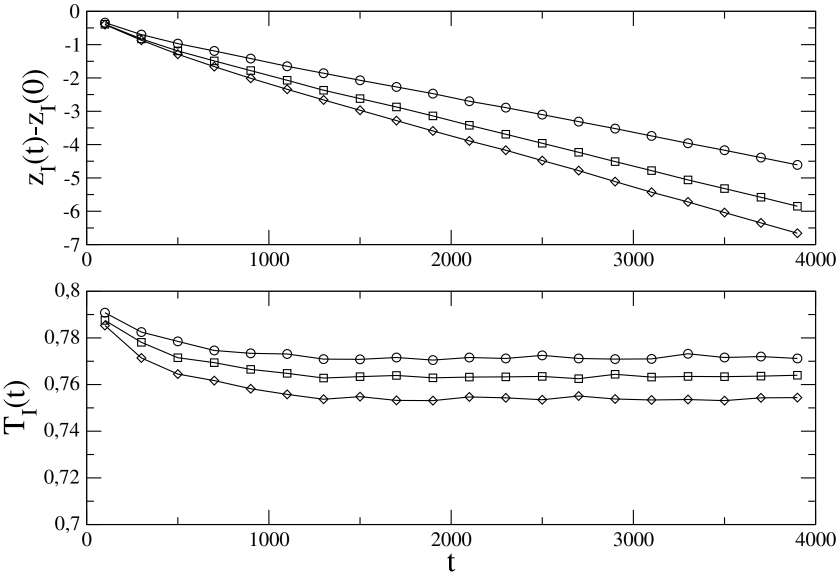

Figure 4: MD computed time evolution of interface position $z_I(t)$ and temperature $T_I(t)$, for $T_l = 0.80$; $v_p = 0.1$ (○), $v_p = 0.15$ (□), $v_p = 0.2$ (◇).

the bulk of the liquid region the density is almost linearly increasing because of the interface evaporative cooling. The upper panel in Figure 4 shows the displacement of the interface position $z_I(t)$ with respect to its initial value $z_I(0)$ as a function of time, for three simulation with temperature $T_l = 0.8$ and $v_p = 0.1, 0.15, 0.20$. The interface position is defined as the point corresponding to the steepest density profile slope. All curves show an initial stage of the evaporation process in which the recession velocity increases till it reaches a fairly constant value. As shown in the lower panel of Figure 4, the initial stage corresponds to the drop of the nominal interface temperature $T_I(t) = T(z_I(t))$, caused by evaporation. After the initial temperature drop, the interface temperature T_I stabilizes when the energy flux associated with evaporation is balanced by the conductive heat flux from the liquid bulk and the interface recession velocity becomes nearly constant. Profiles of the interface structure at time $t = 3900$ is shown in Figure 5. The density profile provides a natural reference to describe the interfacial flowfield. The vertical dashed line marks the "center" of the interface as the position of steepest slope of the density profile. The choice of this reference position is not merely conventional. Actually, the fluid velocity is equal to zero in the liquid bulk but it starts accelerating towards its limit value, v_p, from a position very close to the interface center, as defined above. The temperature profiles show that the same position seems to mark also the beginning of the non-equilibrium region in the vapor expansion. Considering the flow geometry, it is convenient to define the longitudinal and transversal temperatures $T_{\|}$ and $T_{\perp}$ defined as:

$$\begin{aligned} T_{\|}(z,t) &= \frac{1}{Rn(z,t)} \int \left[\xi_z - v_z(z,t)\right]^2 f(\xi,z,t)\, d\xi \qquad (5) \\ T_{\perp}(z,t) &= \frac{1}{2Rn(z,t)} \int \left(\xi_x^2 + \xi_y^2\right) f(\xi,z,t)\, d\xi \qquad (6) \end{aligned}$$

$T_{\|}$ and $T_{\perp}$ are the dispersions of the distribution function $f(\xi, z, t)$ of molecular velocities ξ at position z and time t, respectively along the direction parallel and perpendicular to the net flow velocity $v_z(z,t)$. The overall temperature T is defined as

$$T = \frac{T_{\|} + 2T_{\perp}}{3}$$

.

Within the liquid bulk, the temperatures $T_{\|}$ and $T_{\perp}$ coincide with the value of the overall temperature T which, outside the narrow thermostatted strip, exhibits a linearly decreasing profile. The superposed linear profiles of $T_{\|}$, $T_{\perp}$ and T start separating in the vicinity of the interface center. The longitudinal temperature $T_{\|}$ exhibits the strongest drop in the outermost region of the interface, reaching a minimum at the beginning of the vapor region. The three temperatures relax to a common spatially uniform value T_{∞} in the equilibrium region at the end of the Knudsen layer, where the velocity takes the piston value v_p and the density the uniform value n_{∞}. As discussed in many kinetic theory studies of the Knudsen layer structure close to an evaporating surface [25], the

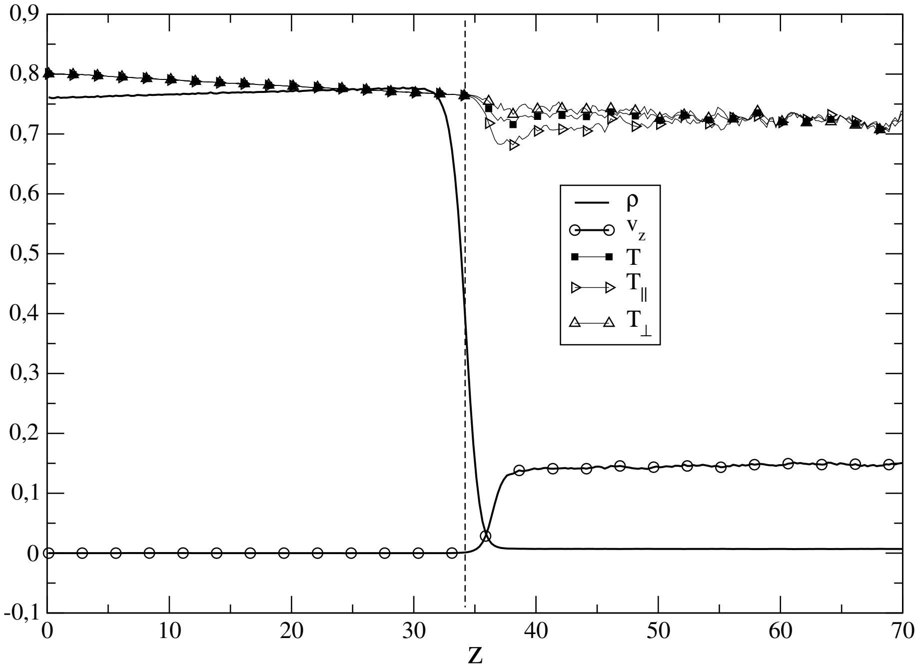

Figure 5: MD computed density, velocity and temperatures profiles at $t = 3900$; $T_l = 0.8$, $v_p = 0.15$. The vertical dashed line marks the position of z_I, coinciding with the maximum of $\left|\frac{\partial\rho}{\partial z}\right|$

.

separation of longitudinal and transversal temperature profiles is caused by the anisotropy of the distribution function $f(\xi, z, t)$. In the vicinity of the liquid surface, f is the superposition of two different molecular streams. The first one, composed by evaporating molecules, has a Maxwellian shape with temperature T_I and virtually zero drift velocity in the half space $\xi_z > 0$ [4]. The second one, composed by molecules traveling toward the liquid surface ($\xi_z < 0$), has a distribution well approximated by a half-space Maxwellian with temperature T_∞ and drift velocity v_p. The resulting f will have different temperatures in the directions normal and parallel to the liquid surface. In particular, $T_\parallel$ will be lower than $T_\perp$ because directly affected by the gas expansion, through v_z. Although a more comprehensive comparison of MD results with the kinetic description of the Knudsen layer will be given in Section 5, it is worth observing that if it is assumed that the evaporation coefficient of the LJ liquid is equal to one and liquid surface is attributed the temperature T_I corresponding to the position z_I defined above, then the MD temperature and density jumps across the Knudsen layer are in good agreement with the prediction of kinetic theory for the evaporation of a monatomic dilute gas [18, 25]. For instance, in the case $T_l = 0.8$, $v_p = 0.2$ (see Fig. 14) the downstream Mach number $M_\infty = v_p/\sqrt{5T/3}$ amounts to about 0.185, whereas $T_I \approx 0.75$. The kinetic theory temperature and density ratios T_∞/T_I and $\rho_\infty/\rho_s(T_I)$ for the given value of M_∞ are respectively equal to 0.93 and 0.77. The corresponding MD values are 0.93 and 0.78, respectively. The density jump has been computed using the equilibrium reduced saturated vapor density $\rho_s(T_I)$ computed from the vapor-liquid coexistence curve derived from Eq. (2), which is in excellent agreement with equilibrium MD data.

4. Diffuse interface model predictions

In 1901, Korteweg [3] proposed to model capillary phenomena by adding, besides pressure, a suitable set of terms depending on the density gradient to the *static* stress tensor $\mathbf{P}^{(s)}$ [1, 2]. In its simpler form [2], $\mathbf{P}^{(s)}$ reads:

$$\mathbf{P}^{(s)} = \left(p - K\rho\nabla^2\rho - \frac{1}{2}K|\nabla\rho|^2\right)\mathbf{I} + K\nabla\rho\otimes\nabla\rho \tag{7}$$

where $p(\rho, T)$ is the hydrostatic pressure in the uniform fluid, given by the fluid equation of state as function of density ρ and temperature T. The coefficient K influences the intensity of the density gradient terms and it is generally a function of both density and temperature. In a state of thermal and mechanical equilibrium, the density field is determined by requiring uniform temperature T and the following condition on the static stress tensor:

$$\nabla\cdot\mathbf{P}^{(s)} = 0 \tag{8}$$

In a one dimensional configuration in thermal and mechanical equilibrium, with an infinite planar interface separating the liquid and vapor phases, the fluid density depends only on the spatial coordinate z, normal to the interface. In this case, with the static stress tensor given by Eq. (7), Eq. (8) states that the $P_{zz}^{(s)}$ component is constant throughout the fluid:

$$P_{zz}^{(s)} = p - K\frac{d^2\rho}{d\,z^2} + \frac{1}{2}K\left(\frac{d\,\rho}{d\,z}\right)^2 = p_\infty \tag{9}$$

Eq. (9) determines the density profile; p_∞ is a boundary condition and it is computed imposing the usual thermodynamic condition for phase equilibrium. The coefficient K is related to the surface tension γ by the relationship:

$$\gamma = \int_{-\infty}^{\infty} K\left(\frac{d\,\rho}{d\,z}\right)^2 dz \tag{10}$$

The extension of Korteweg theory to non-equilibrium flows can be modeled by the conservation laws of mass, momentum and energy [1, 2]:

$$\frac{\partial\rho}{\partial t} + \nabla\cdot(\rho\vec{v}) = 0 \tag{11}$$

$$\frac{\partial\rho\vec{v}}{\partial t} + \nabla\cdot(\rho\vec{v}\otimes\vec{v} + \mathbf{P}) = 0 \tag{12}$$

$$\frac{\partial\rho e_T}{\partial t} + \nabla\cdot(\rho e_T\vec{v} + \mathbf{P}\cdot\vec{v} + \vec{q}) = 0 \tag{13}$$

with the following closures:

$$\rho e_T = \rho e + \frac{1}{2}K|\nabla\rho|^2 + \frac{1}{2}\rho v^2 \tag{14}$$

$$\mathbf{P} = \mathbf{P}^{(s)} + \boldsymbol{\tau} \tag{15}$$

$$\boldsymbol{\tau} = -\mu\left(\nabla\vec{v} + \nabla\vec{v}^T\right) - \eta\left(\nabla\cdot\vec{v}\right)\mathbf{I} \tag{16}$$

$$\vec{q} = -\lambda\nabla T + K\rho\left(\nabla\cdot\vec{v}\right)\nabla\rho \tag{17}$$

As shown by Eq. (14), the total fluid energy per unit mass, e_T, is obtained by adding the contribution of capillary forces, $1/2K|\nabla\rho|^2$, to the sum of the fluid kinetic energy and internal energy $e(\rho, T)$ of the uniform fluid. The total stress tensor $\mathbf{P}$ is defined in Eq. (15) by adding to the Korteweg contribution, $\mathbf{P}^{(s)}$, the viscous stress $\boldsymbol{\tau}$ in the usual Navier-Stokes form. In Eq. (16), μ is the coefficient of shear viscosity and η the coefficient of volume viscosity. The quantity $\vec{q}$ in Eq. (17) denotes the total heat flux, consisting of the classical

Fourier law contribution, $-\lambda\nabla T$, λ being the thermal conductivity and a capillary contribution, $K\rho\,(\nabla\cdot\vec{v})\,\nabla\rho$, often referred to as interstitial working, in literature [1]. Under the main assumption that the Clausius-Duhem inequality and the usual thermodynamic relationships among internal energy, entropy and Helmoltz free energy are valid also inside the non-uniform interface region [1], the above closures ensure that the production term in the entropy balance equation is non-negative [2].

It is to be observed that the introduction of the Korteweg capillary stress model into the Eqs. (11-14) allows for a physically realistic description of interfacial phenomena, therefore the characteristic space and time scales of the model become comparable to those of atomistic simulations. In order to build up a Diffuse Interface Model consistent with the properties of the Lennard-Jones (LJ) fluid, the equations of state $p = p(\rho, T)$ and $e = e(\rho, T)$ have been computed from the modified Benedict-Webb-Rubin form, proposed in Ref. [14], which allows an accurate representation of MD data in a wide range of density and temperature (the form of the pressure is given by Eq. 2). Moreover, simple mean field corrections allow accurately adding the dependence of thermodynamic properties on the LJ potential cutoff distance r_c [14]. Shear viscosity $\mu(\rho, T)$ and thermal conductivity $\lambda(\rho, T)$ have been computed from the expressions given in Ref. [15] and Ref. [16], respectively. The proposed correlations exhibit a maximum error of 3.2% and an average error of 1.2% for thermal conductivity, whereas a maximum error of 5.0% and an average error of 1.9% holds in the case of viscosity. Errors are intended as deviation from MD data sets used to obtain the correlation themselves. The contribution of volume viscosity to normal stresses has been neglected because the results suggested that the vapor expansion occurs mainly in the low density flow region where volume viscosity is small. In most of the calculations presented here, the coefficient $K(\rho, T)$, appearing in Eq. (7), has been assumed not to depend on the density ρ, although its value has been made to depend on T_l. For each computed solution, $K(T_l)$ has been obtained by matching the MD computed equilibrium density profile with the DIM density profile resulting from the integration of Eq. (9). For all considered

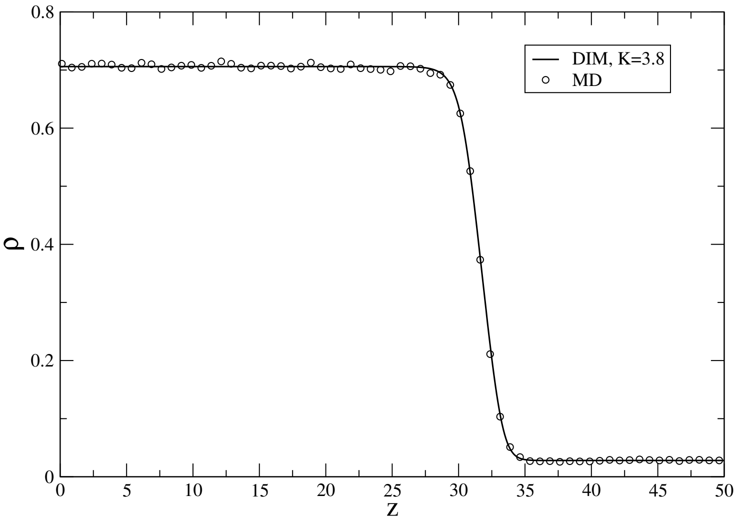

Figure 6: $T_l = 0.90$. Comparison of DIM and MD equilibrium density profiles. Solid line: DIM, $K = 3.8$; ∘: MD.

cases, excellent agreement between equilibrium DIM and MD density profiles has been obtained by a proper choice of $K(T_l)$, as shown in Figure 6. Appendix A provides a more detailed description and discussion about the determination of $K(T_l)$ and the sensitivity of the computations with respect to its setting. It also worth observing that the DIM computed equilibrium liquid and vapor densities are computed from the liquid-vapor coexistence curve obtained from Eq. (2). Hence, the good agreement observed in Figure 6 is also a result of the capability of Eq. (2) to describe MD equilibrium states.

The numerical solution of the governing equations (11), (12) and (13) is not trivial. They form a system of conservation laws with the same formal eigenvalues structure of the Euler equations for a perfect gas. We observe that for sufficiently low values of pressure, the vapor phase behaves practically as a perfect gas. However the equation of state of the Lennard-Jones fluid, unlike the one of the perfect gas, is non-convex for values of the density found inside the interface region. Moreover the fluid can be compressible in the vapor region, but it is practically incompressible in the liquid region. An effective numerical

	v_p	$v_I\times$ 10^3			$\rho_\infty/\rho_s(T_l)$			T_∞/T_l		
		MD	DIM	HM	MD	DIM	HM	MD	DIM	HM
$T_l = 0.80$	0.10	1.00	0.54	1.00	0.66	0.38	0.65	0.93	0.975	0.925
	0.15	1.35	0.6	1.35	0.57	0.26	0.56	0.90	0.96	0.90
	0.20	1.5	0.63	1.5	0.48	0.20	0.48	0.87	0.95	0.87
$T_l = 0.85$	0.1	1.67	1.01	1.66	0.65	0.4	0.65	0.92	0.96	0.92
	0.15	2.15	1.17	2.12	0.57	0.304	0.56	0.89	0.948	0.89
	0.2	2.52	1.26	2.48	0.50	0.25	0.496	0.86	0.94	0.86
$T_l = 0.90$	0.1	2.33	1.67	2.3	0.60	0.44	0.60	0.90	0.944	0.90
	0.15	2.96	1.92	2.97	0.52	0.336	0.51	0.88	0.930	0.87
	0.2	3.45	2.10	3.4	0.45	0.27	0.45	0.85	0.918	0.84

Table 2: MD, DIM and HM predictions of interface velocity v_I, density drop ratio $\rho_\infty/\rho_s(T_l)$ and temperature drop ratio T_∞/T_l as a function of piston speed v_p, for $T_l = 0.80, 0.85, 0.90$. The saturated vapor reduced density $\rho_s(T_l)$ has been computed from the liquid-vapor coexistence curve based on Eq. (2).

scheme able to handle both compressible and incompressible flows is proposed in Ref. [26]. The original scheme is devised for a perfect gas, but it is straightforward to extend it to a Lennard-Jones fluid with a non-convex equation of state. The governing equations (11), (12) and (13) are discretized with a finite volume method over a staggered one dimensional grid. The mass fluxes that transport momentum and energy are computed from the discretization of continuity equation (11), in such a way momentum and energy, besides mass, are conserved [27]. The transport terms associated with the tensor $\mathbf{P} = \mathbf{P}^{(s)} + \boldsymbol{\tau}$ and the heat flux vector $\vec{q}$ are discretized with a central second order approximation. The discretization of the convective fluxes $\rho\vec{v}$, $\rho\vec{v}\otimes\vec{v}$ and $\rho\vec{v}e_T$ is more critical. The DIM method, by construction, fully resolves the interface region between the gas phase and the liquid phase. However inside the interface strong density gradients are present. It is well known that under these conditions a central discretization of the convective fluxes can cause unphysical oscillations of the numerical solution [28, 27]. Therefore the convective fluxes are discretized with the second order, non-linear, total variation bounded, OSPRE scheme [29], that ensures a non-oscillatory behaviour of the numerical solution. The OSPRE scheme uses a three point stencil to compute the convective fluxes. The stencil is locally upwind-biased [29] with respect to the direction of fluid velocity, in this way the scheme can be used also in regions where the equation of state is non-convex. As a check of the accuracy of the OSPRE scheme, we have computed the evaporation process, for $T_l = 0.8$ $v_p = 0.15$, also with a second order central discretization of the convective fluxes: the maximum relative difference between the two computations is less than 1.5 %.

The discretized governing equations are advanced in time with an explicit, second order accurate Runge-Kutta strong stability preserving method [30]. The choice is dictated by the nonlinear stability properties that the above scheme enjoys for the numerical solution of systems of conservation laws with discontinuities or strong gradients. The second order Runge-Kutta method is stable if the Courant-Friedrichs-Lewy (CFL) number is equal or smaller than one. The time step of the numerical integration is chosen in order to respect the CFL number condition. The governing equations (11), (12) and (13) contain both convective terms and diffusive terms and each of them imposes its own restriction on the time step [27]. At every time step the most restrictive condition is chosen and the time increment computed from the requirement $CFL \leq 1$ is used to advance the numerical solution.

The one dimensional domain is divided into N_c cells; because the finite volume method is staggered, density and energy unknowns are located at the cells center, while velocity is located at the cells faces. In the computations presented here all the cells have the same width. However it is possible to have cells of variable width, with smaller cells in the interface region and larger cells in the bulk regions, in order to reduce the total number of cells and the computational time. For the computations presented in this contribution we have performed a grid refinement study in order to assess the optimal number of grid points by using a simple criteria: we have enough grid points when increasing their

		MD			DIM	
T_l	T_∞	ρ_∞	$v_I \times 10^3$	T_∞	ρ_∞	$v_I \times 10^3$
0.80	0.744	8.09e-03	1.0	0.78	4.66e-03	0.54
0.85	0.788	1.23e-02	1.7	0.815	7.6e-03	1.0
0.90	0.819	1.68e-02	2.5	0.847	1.192e-02	1.675
0.95	0.843	2.08e-02	3.12	0.869	1.557e-02	2.29
1.00	0.873	2.631e-02	3.923	0.893	2.06e-02	3.31
1.05	0.90	3.275e-02	5.357	0.916	2.564e-02	4.22

T_l	$\Delta T/T_\infty^{(MD)}$	$\Delta \rho/\rho_\infty^{(MD)}$	$\Delta v_I/v_I^{(MD)}$
0.80	5.0e-02	0.42	0.46
0.85	3.4e-02	0.38	0.41
0.90	3.1e-02	0.29	0.33
0.95	2.7e-02	0.25	0.27
1.00	2.3e-02	0.22	0.19
1.05	1.8e-02	0.22	0.21

Table 3: **Upper part**- MD and DIM predictions of interface velocity v_I, downstream density ρ_∞ and temperature T_∞, as functions of T_l for fixed piston speed $v_p = 0.1$. **Lower part**- Relative deviation of DIM v_I, T_∞ and ρ_∞ from corresponding MD data.

number by 50 % changes the solution by less than 1 %. Boundary conditions are imposed with a layer of two ghost cells at each boundary of the domain. On the vapor side of the domain, velocity is specified by the boundary condition, density and energy are extrapolated from the interior with the condition of zero gradient. On the liquid side of the domain, temperature is imposed, density is extrapolated from the interior assuming that it is symmetric, velocity is extrapolated assuming that it is antisymmetric.

4.1. Numerical results

Equations (11-13) have been numerically solved by the scheme described above to study the test problem formulated in Section 2 with the same physical

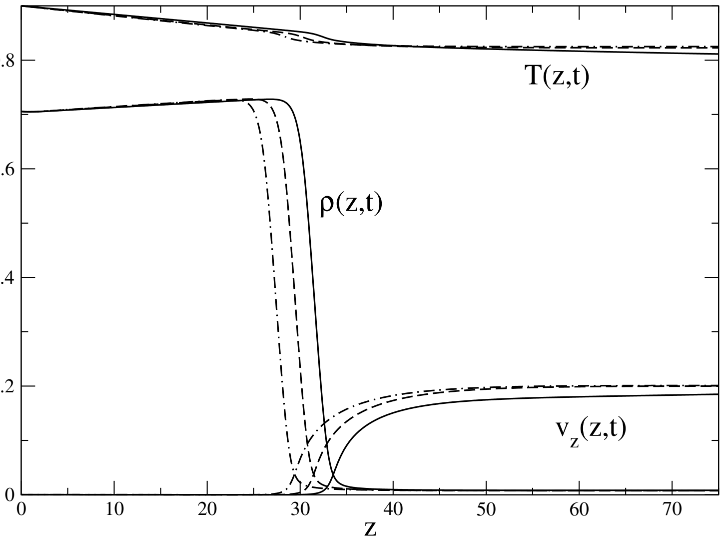

Figure 7: $T_l = 0.90$,$v_p = 0.2$. Time evolution of DIM computed density, temperature and velocity fields.

setting adopted for MD simulations. However, the DIM computational setup presents some differences with respect to MD. First of all, the spatial symmetry of the problem has been fully exploited in DIM by computing the solution only in the half space $z > 0$. Secondly, the extent of DIM spatial domain has been kept constant in time. The piston used in MD simulations has been replaced by an open boundary in the vapor region, where the boundary conditions described above have been assigned. If the distance of the open boundary from the liquid-vapor interface is large enough to contain the region where the vapor expand into a downstream uniform flow with prescribed velocity v_p, then the system will exhibit the same long time behavior observed in MD simulations, although the initial transient will be different. In particular, after the initial cooling phase the interface temperature will remain fairly constant for a time sufficiently long to allow the development of a quasi-stationary vapor flowfield. Moreover, the interface will recede with constant velocity while keeping the same structure. Figure 7 shows the time evolution of DIM computed density, temperature and velocity fields in the case $T_l = 0.90$ and $v_p = 0.2$. The solid lines represent the

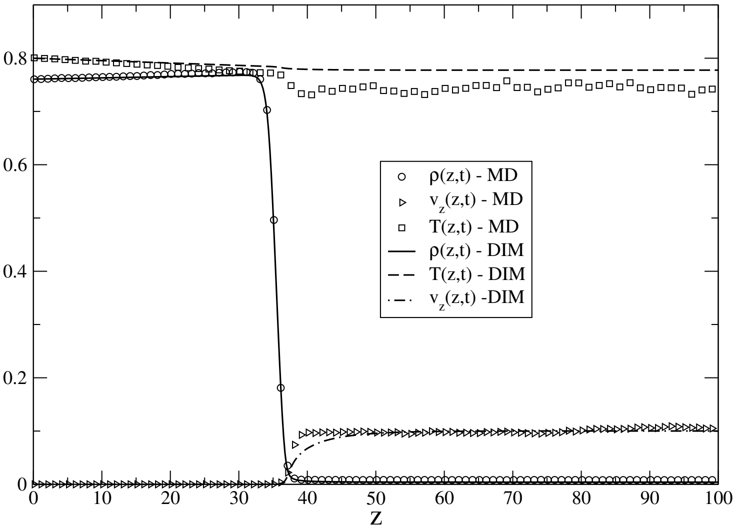

Figure 8: $T_l = 0.80$,$v_p = 0.1$. Comparison of MD and DIM computed density, temperature and velocity fields.

solution at a time belonging to the transient phase, whereas the dashed and dot-dashed lines are associated to two successive profiles taken after the downstream flowfield has reached its asymptotic uniform and quasi stationary state. Although the description of the liquid film evaporation provided by the diffuse interface model is qualitatively in agreement with MD one, the quantitative comparison shows discrepancies depending on the physical system setting. Figures 8 and 9 show the comparison of MD and DIM flowfield profiles in two cases with the same temperature, $T_l = 0.80$, but different downstream velocities, respectively $v_p = 0.1$ and $v_p = 0.2$. In each figure, MD and DIM are compared at the time when both system have reached their respective quasi-stationary condition with coincident interface positions. Since the downstream velocity is assigned in both computational schemes, the downstream value of $v_z(z,t)$ is the same. However, the approach to the asymptotic limit is different. The MD velocity profile has a much sharper jump to v_p. In the case of the temperature and density, the discrepancy is not limited to the length scale of the approach to the asymptotic value but involves the respective downstream values T_∞ and

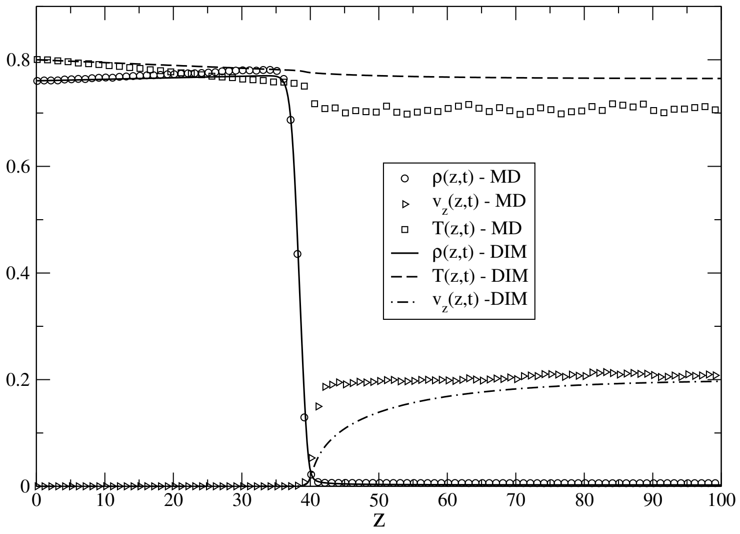

Figure 9: $T_l = 0.80$,$v_p = 0.2$. Comparison of MD and DIM computed density, temperature and velocity fields.

ρ_∞. DIM predicts smaller temperature jumps and larger density jumps. The discrepancies are larger for larger values of v_p. Since DIM predicts lower values of ρ_∞ for the same v_p, DIM overall evaporation rates and interface recession velocity will be accordingly lower than the respective MD data. Table 2 summarizes MD and DIM computed values of the interface recession velocity v_I, asymptotic temperature T_∞ and density ρ_∞, respectively normalized to T_l and the saturated vapor density $\rho_s(T_l)$, for the three lowest values of T_l where the vapor is close to ideal conditions. The comparison clearly indicates that the large discrepancy between the predicted values of ρ_∞ causes DIM to strongly underestimate v_I. However, the discrepancies seem to become smaller as T_l grows and the vapor becomes accordingly denser, as shown in Table 3 reporting the values of T_∞, ρ_∞ and v_I as a function of T_l, for $v_p = 0.1$. In the lower part of the table, the relative deviations, normalized to the MD values, are shown. The smaller discrepancies at higher T_l are also evident in the flowfield comparison presented in Figure 10, showing the case $T_l = 1.05$, $v_p = 0.1$. Now the asymptotic temperature discrepancy is quite small and the velocity profiles

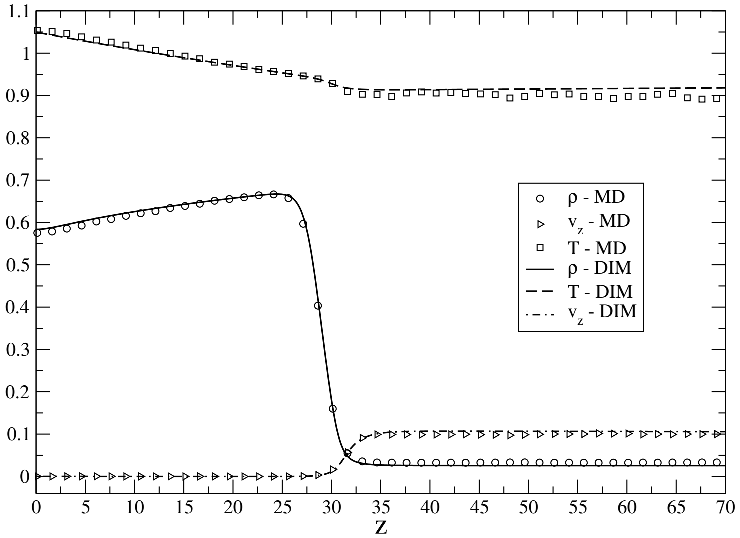

Figure 10: $T_l = 1.05$, $v_p = 0.1$. Comparison of MD and DIM computed density, temperature and velocity fields.

very close. Again, vapor density exhibits the largest relative error affecting the interface recession velocity discrepancy. As mentioned above, the DIM numerical results have been obtained using a constant value of K, as assumed in many previous studies. Although the dependence of K on density and temperature can be explicitly obtained for simplified kinetic models [31], its derivation, even approximate, is much more difficult for the LJ fluid [32]. Hence, the sensitivity of the numerical results has been explored by imposing artificial variations of K in two ways. In the first one [13] the nominal value of $K_{nom}(T_l)$ was simply given a different constant value within a 20% error band. In the second one, K, μ and λ have been assumed to depend on the density gradient, which appreciably changes the considered quantities only in the interface region. A similar method has been used in Ref. [9] to introduce perturbations in the transport properties within the interface region, where the density rapid changes might invalidate the assumptions leading to hydrodynamic equations. The results, reported in Appendix A, show little changes with respect to nominal ones, indicating that the severe discrepancies observed at low values of T_l cannot be corrected by moderate perturbations of DIM fluid properties.

5. Hybrid model

In order to highlight the importance of kinetic effects in the Knudsen layer next to evaporating liquid surface and to assess the accuracy of the kinetic boundary conditions at the liquid-vapor interface, the evaporation of the liquid film has also been studied by a hybrid model in which the liquid is described by hydrodynamic equations, whereas the vapor is assumed to be governed by the Boltzmann equation. At variance with the two approaches described in Sections 3 and 4, the interface has no structure, being replaced by a plane, separating the liquid and vapor phases, where the boundary conditions described below are assigned. Such treatment of the interface is consistent with the use of a kinetic model, the Boltzmann equation, whose natural spatial and time scales are the mean free path and free time in an *assumed* ideal gas, where the said kinetic scales are much larger than molecular size and molecular interaction time, respectively. Hence, when comparing MD with HM calculations, it should be considered that, although the gas number density are tuned to be the same, the way DSMC deals with atomic collisions leads to an ideal gas behavior by construction. Comparisons are therefore justified at low T when the MD simulated vapor is closer to the ideal gas condition. In the hybrid model description, the fluid occupies a parallelepiped of constant area S and height $z_p(t)$, the latter being the piston position at time t. The origin of the coordinate system is located in the center of the liquid slab extending up to the interface position $z_I(t)$. Accordingly, the vapor occupies the volume extending from $z_I(t)$ to $z_p(t)$.

The very small macroscopic velocity $v_z^{(l)}$ in the liquid bulk due to the thermal expansion/contraction of the liquid, can be neglected. Hence, the mass conservation at the interface position can be written as:

$$-\rho^{(l)} v_I = \dot{m} = m \int (\xi_x - v_I)\, f(z_I, \xi, t)\, d\xi \tag{18}$$

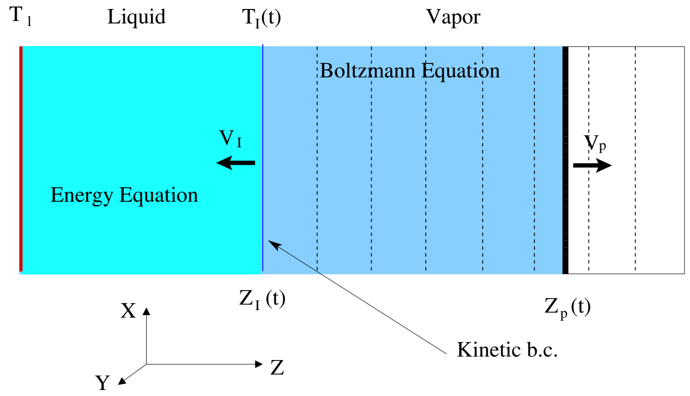

Figure 11: Sketch of the computational domain of the hybrid model simulations. Vertical dashed lines schematically represent the spatial grid cell system of the DSMC algorithm describing the vapor phase.

A further consequence of the absence of appreciable motion within the liquid film is that the $P_{zz}^{(l)}$ component of the stress tensor is uniform and equal to the hydrodynamic pressure $p^{(l)}(\rho^{(l)}, T^{(l)})$. Equality of momentum flux along z on the liquid and vapor sides of the interface leads to the following relationship at $z = z_I$

$$P_{zz}^{(l)} = m \int \xi_z \left(\xi_z - v_I\right) f(z_I, \xi, t)\, d\xi \tag{19}$$

which determines the pressure in the liquid from the molecular momentum flux on the vapor side of the interface. The temperature field $T^{(l)}(z,t)$ in the liquid is determined by the energy equation which takes the following form:

$$\rho^{(l)} C_p \frac{\partial T^{(l)}}{\partial t} = \frac{\partial}{\partial z}\left(\lambda \frac{\partial T^{(l)}}{\partial z}\right) \tag{20}$$

Eq. (20) is solved by assigning the constant temperature $T^{(l)}(0,t) = T_0^{(l)}$ in the center of the liquid slab and the energy flux at $z = z_I$, obtained by the relationship:

$$-\lambda \frac{\partial T^{(l)}}{\partial z} - \rho^{(l)} v_I e^{(l)}(\rho^{(l)}, T^{(l)}) = \frac{m}{2} \int \xi^2 \left(\xi_z - v_I\right) f(z_I, \xi, t)\, d\xi \tag{21}$$

expressing equality of energy fluxes on the liquid and vapor sides of the interface. The spatially one-dimensional Boltzmann equation:

$$\frac{\partial f}{\partial t}+\xi_z\frac{\partial f}{\partial z}=\frac{\sigma_{hs}^2}{2}\int\left[f(z,\xi_1^*,t)f(z,\xi^*,t)-f(z,\xi_1,t)f(z,\xi,t)\right]\|\hat{\mathbf{k}}\circ\xi_r\|\,d^2\hat{\mathbf{k}}\,d\xi_1 \tag{22}$$

for a dilute gas of hard spheres of diameter σ_{hs}, is assumed to govern the vapor phase flowfield. In Eq. (22), $\hat{\mathbf{k}}$ is a unit vector which assigns the relative position of two colliding atoms at the time of their impact with velocities ξ, ξ_1 and relative velocity $\xi_r=\xi_1-\xi$. The velocities ξ^* and ξ_1 respectively transform into ξ, ξ_1 in a restituting collision [17] according to the following expressions:

$$\xi^*=\xi+(\hat{\mathbf{k}}\circ\xi_r)\hat{\mathbf{k}} \tag{23}$$

$$\xi_1^*=\xi_1-(\hat{\mathbf{k}}\circ\xi_r)\hat{\mathbf{k}} \tag{24}$$

To match the effective collision cross section of the Lennard-Jones interaction, σ_{hs} has been computed from shear viscosity $\mu(T_0^l)$ of the Lennard-Jones dilute by Eq. (3), to ensure that at the temperature $T_0^{(l)}$ the hard sphere gas described by Eq. (22) has the same shear viscosity of the Lennard-Jones gas. Since the temperature changes in the flowfield are small, the above setting will produce very close kinetic relaxation rates in the Knudsen layer for the two fluid models. It is also to be stressed that the jumps suffered by macroscopic quantities across the kinetic layer are fairly insensitive to the assumed intermolecular potential [33]. Boundary conditions for Eq. (22) are prescribed at the liquid vapor interface and at the moving piston surface. Following a quite standard formulation of kinetic boundary conditions at evaporating surfaces [4], it is assumed that atoms emitted from the liquid surface into the gas phase are distributed according to the following half-range Maxwellian:

$$f_I=\frac{\sigma_e n_s(T_I)+(1-\sigma_e)n_r}{(2\pi RT_I)^{3/2}}\exp\left\{-\frac{\xi^2}{2RT_I}\right\}\quad \xi_z>0 \tag{25}$$

$$n_r=\sqrt{\frac{2\pi}{RT_I}}\int(\xi_z-v_I)\,f(z_I,\xi,t)\,d\xi \tag{26}$$

In Eq. (25), σ_e is the evaporation coefficient, $n_s(T_I)$ the equilibrium saturated vapor density at the temperature T_I, whereas n_r is the number density associated with the atoms of the vapor which are ”reflected” back into vapor phase after being scattered by the liquid. As is evident, Eq. (25) assumes that the reflected component is diffusively scattered with the same probability of the spontaneously evaporating atoms.

The piston is assumed to be specularly reflecting hence, only the z component of the velocity is affect by an atom-piston collision, being changed from ξ_z to $\xi_z' = -\xi_z + 2v_p$.

5.1. Numerical Implementation

The evolution of the system has been computed by dividing the total simulation time into a number of time steps of equal duration Δt. At each time step liquid and vapor flowfields have been obtained from Eqs. (20,22), taking into account the boundary conditions described above. The Boltzmann equation has been solved numerically by a quite standard implementation of the Direct Simulation Monte Carlo (DSMC) method [34]. The DSMC scheme has been based on a rigidly translating spatial grid of fixed length L_z and divided into a fixed number of spatial cells. The left grid boundary coincides with the position $z_I(t)$ of the liquid-vapor interface. The piston is allowed to move through the grid and, at a given time t, it divides the cell containing its current position into two parts, one of which is empty. The piston motion momentarily distorts the sampling of macroscopic quantities in the cell it occupies. However, this is not a problem once the piston is far from the liquid surface and the Knudsen layer completely developed. The typical spatial cell size has been set to 1/10 of the equilibrium mean free path in the vapor at the reference temperature T_l. The typical used time step Δt is 1/20 of the mean free time. In order to obtain accurate time resolved flowfield profiles, a high number of particles per cell has been used, usually more that 5000, by setting the domain section S to have the same vapor number density of the companion MD simulation. Moreover, macroscopic quantities have been computed averaging particles microscopic states over a short time interval,containing several time steps. The sampling time duration has been set short enough to make the grid motion, due the slow interface recession, negligible. The DSMC step is executed first, in order to obtain the mass, momentum and energy fluxes appearing in Eqs. (18,19,21) and used for the computation of the temperature and density in the liquid.

Eq. (20) is solved in the liquid region, occupying the interval $[0, z_I(t)]$. In order to take into account the liquid density variations due to the non-uniform temperature of the liquid film, the liquid region is initially divided into a number of cells having the same size and the same mass. Then, the computation of the temperature and density fields is splitted into two main substeps. First Eq. (20) is solved by a simple time implicit and conservative finite difference centered scheme, using the constant volume specific heat per unit mass, C_v, in place of the specific heat at constant pressure. More precisely, a provisional temperature value T_i' is computed computed in the $i-th$ cell at time $t+\Delta t$, as:

$$T_i'(t+\Delta t) = T_i'(t) + \frac{\Delta Q_i}{C_v} \tag{27}$$

where, for internal cells, ΔQ_i is the heat the $i-th$ cell exchanges with the surrounding ones by conduction, at constant volume (and density). For the outermost cell, ΔQ_i includes the energy exchanged with the vapor phase, according with Eq. (21). After this first substep, the pressure $p_i' = p(\rho_i, T_i')$ is not equal to the desired constant value $P_{zz}^{(l)}$, being $\Delta p_i = p_i' - P_{zz}^{(l)}$ the pressure excess. The pressure in the liquid is then relaxed to $P_{zz}^{(l)}$ by an adiabatic transformation (heat exchange has already been taken into account) in which the volume of each cell is changed to obtain constant pressure, equal to $P_{zz}^{(l)}$. This achieved by performing a second substep in which the cell temperature and density are given the following variations, respectively:

$$\Delta T_i = -\left[\frac{\frac{p}{\rho^2} - \frac{\partial e}{\partial \rho}}{\frac{\partial p}{\partial \rho}\frac{\partial e}{\partial T} + \frac{\partial p}{\partial T}\left(\frac{p}{\rho^2} - \frac{\partial e}{\partial \rho}\right)}\right]_i^{(l)} \Delta p_i \tag{28}$$

$$\Delta \rho_i = \left[\frac{\frac{\partial e}{\partial T}}{\frac{p}{\rho^2} - \frac{\partial e}{\partial \rho}}\right]_i^{(l)} \Delta T_i \tag{29}$$

The addition of ΔT_i to T_i' in each cell provides the temperature field in the liquid slab at time $t+\Delta t$. The updated density is $\rho_i(t+\Delta t) = \rho_i(t) + \Delta\rho_i$ and

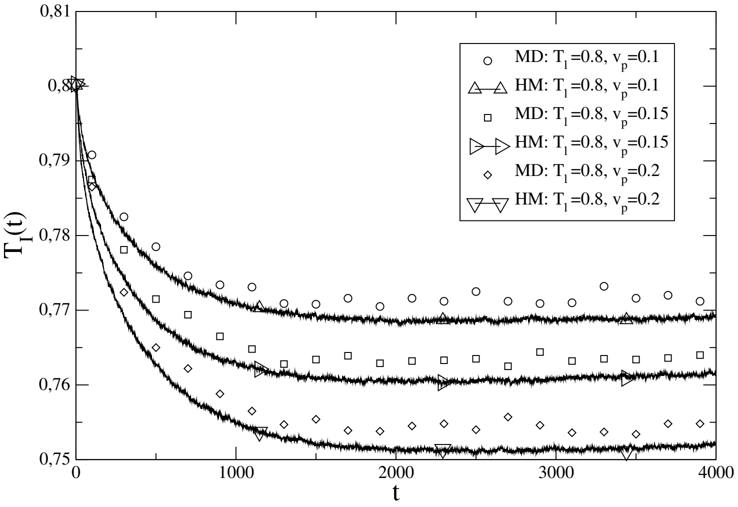

Figure 12: Comparison of MD and HM computed time evolution of interface temperature T_I. $T_l = 0.8$, $v_p = 0.1, 0.15, 0.2$. In HM, $\sigma_e = 1$ is assumed.

the updated cell size is $\Delta z_i = \Delta m_i/(S\rho_i)$, where Δm_i and S are the mass of cell i and liquid column section, respectively. Finally, the size and mass of the last cell, bounded by the interface is changed according to Eq. (18). When the size of the outermost cell of the liquid domain falls below a prescribed threshold, the cell is merged with the preceding one, summing the masses of the two merged cells and computing a new average cell temperature which keeps the internal energy unchanged after the merging. The interface position z_I is obtained by summing all cell sizes Δz_i.

5.2. Numerical results

The comparisons between MD and HM results have been limited to the cases $T_l = 0.80, 0.85, 0.90$. As shown in Table 1, even for the lowest temperature value the vapor is slightly non-ideal. However, the surface cooling caused by evaporation and the vapor expansion tend to lower the vapor density. Hence, in the MD computed vapor flows the effective mean free path will be larger and compressibility closer to one than in the indicative equilibrium values given in Table 1, thus bringing MD simulation conditions closer to DSMC vapor flow

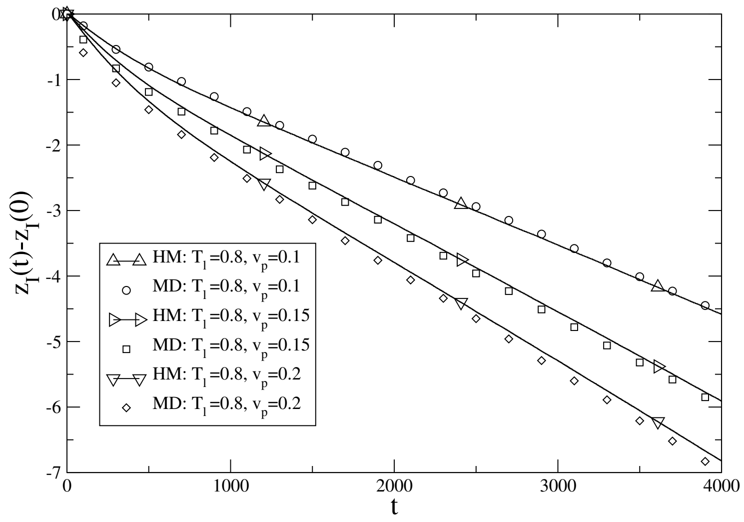

Figure 13: Comparison of MD and HM computed interface recession history z_I. $T_l = 0.8$, $v_p = 0.1, 0.15, 0.2$. In HM, $\sigma_e = 1$ is assumed.

simulations, based on the ideal gas assumption.

Figures 12 and 13 shows the comparisons of MD and HM calculations of interface temperature T_I and displacement $z_I(t) - z_I(0)$ with respect to the initial interface position, respectively. The temperature T_l is equal to 0.80. The initial liquid slab thickness of MD simulations is 80σ for the piston speeds $v_p = 0.1, 0.15$ and 90σ for $v_p = 0.2$. HM results have been obtained setting the evaporation coefficient σ_e equal to one. As mentioned in Section 3, the interface position and temperature for MD simulations is obtained from the point of the steepest density slope. In the case of HM, T_I and z_I are the temperature and position of the right boundary of the outermost cell of the liquid domain, respectively. The HM predicted interface temperature is very close to the corresponding MD results for all considered values of v_p. In general, the hybrid model tend to underestimate MD interface temperature but it should be noted that the largest relative error in the temperature plateau region amounts to about 0.5%. The agreement of the liquid film interface displacement histories is also very good, indicating that the evaporation rates predicted by the two models are very close. The

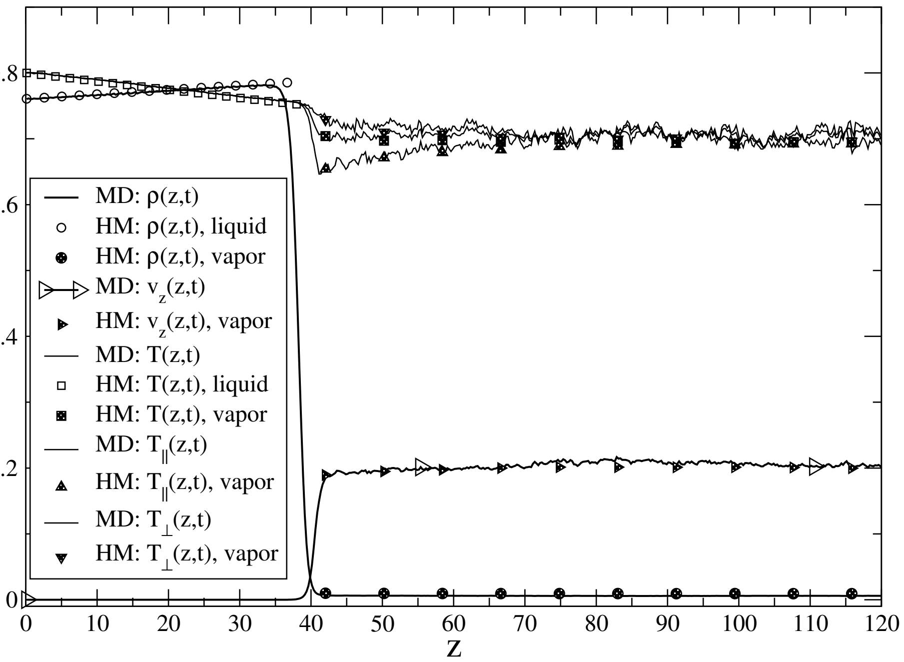

Figure 14: $T_l = 0.8$, $v_p = 0.2$. Comparison of MD and HM flowfields in the Knudsen layer, at time $t = 3900$. In HM, $\sigma_e = 1$ is assumed.

good performances of HM is not limited to the lowest temperature, as shown in Table 2 which reports the interface recession velocities v_I as a function of piston speed and liquid temperature. The reported v_I values have been obtained by linear regression of z_I data in the time window where T_I is nearly constant.

A comparison of density, velocity and temperature profiles computed by the two models is shown in Figure 14, in the case $T_l = 0.8$, $v_p = 0.2$. The flowfields profiles has been taken close to the end of temperature plateau ($t = 3900$). The slow and uniform motion of the interface and the nearly constant value of T_I cause the formation of a quasi-stationary Knudsen layer which translates, following the interface. HM liquid bulk density and temperature profiles agree with the corresponding MD profiles. It should be noted that in the hybrid model the interface region has zero thickness and that the density profiles extends up to the middle of the MD computed interface, where the liquid density is much lower. The HM vapor density, velocity and temperatures $(T, T_{\parallel}, T_{\perp})$ are all very close to the corresponding MD profiles. Again, to superpose HM and MD vapor profiles it is necessary to take into account the finite extent of the MD interface and shift the HM profiles to the position of the minimum of $T_{\parallel}$, which provides a good approximation for the beginning of the kinetic layer in the dilute vapor region [20].

Table 2 also reports the uniform density and temperature values, respectively ρ_{∞} and T_{∞}, at the end of the Knudsen layer, where the expansion turns into a uniform equilibrium flow. The reported density values are normalized to the vapor saturation density $\rho_s(T_l)$, whereas T_{∞} values are normalized to T_l. Both HM and MD density and temperature jumps are in good agreement for all the considered combinations of piston velocity and bulk liquid temperature. Although HM predictions are close to MD results for $\sigma_e = 1.0$, it is of some interest to explore the sensitivity of the HM result to changes of the evaporation coefficient. A few exploratory simulations have been performed with $\sigma_e = 0.8, 0.9$, assuming that the fraction $1 - \sigma_e$ of vapor atoms impinging on the interface are diffusely re-emitted into the vapor phase. Values of σ_e close to unity have been chosen on purpose to match suggestions from previous numerical studies on monatomic fluids [31, 5]. Figures 15 and 16 respectively show the interface temperature $T_I(t)$ and displacement $z_I(t) - z_I(0)$ histories, for the case $T_l = 0.8$, $v_p = 0.2$. The HM computed curves for $\sigma_e = 0.8, 0.9, 1.0$, are compared with MD data. First of all, it should be noted that the variation of σ_e has a limited effect on the surface temperature and evaporation rate. The system responds as expected: the lower evaporation rate obtained by reducing σ_e, produces slightly higher surface temperature and lower recession velocity. The data seem to favor the choice $\sigma_e = 1.0$, because of the better agreement with MD surface recession data. Although the HM simulation with $\sigma_e = 0.8$ has a better agreement with the MD $T_I(t)$ curve, it should be noted that the interface temperature associated with MD simulations has a more conventional nature.

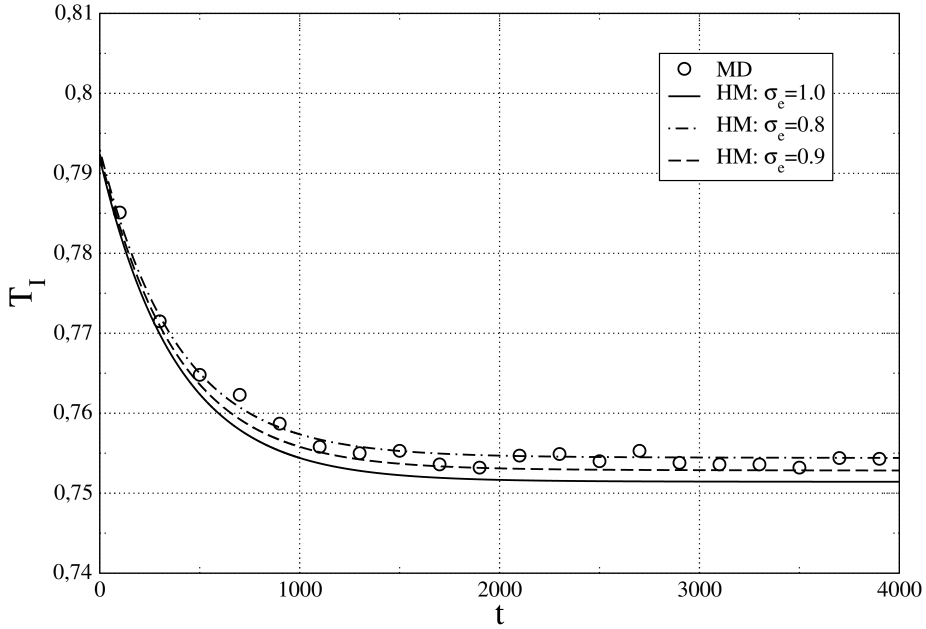

Figure 15: $T_l = 0.8$, $v_p = 0.2$. Effect of evaporation coefficient on $T_I(t)$ curve. Diffuse re-emission of reflected vapor flux is assumed.

6. Concluding remarks

The evaporation of a thin liquid film has been used as a test problem to assess the capabilities of a diffuse interface model and hybrid continuum-kinetic model to reproduce benchmark solutions, obtained by molecular dynamics simulations of the Lennard-Jones fluid. The results show that diffuse interface models solutions deviate from MD simulation results when the vapor phase is dilute and rarefaction effects are more pronounced. Discrepancies tend to become smaller when the vapor phase become denser. On the contrary, the hybrid model, whose applicability is limited to cases where the vapor phase is dilute, shows a fairly good agreement with MD simulations when the evaporation coefficient is between 0.8 and 1.0. The results also indicate that some modifications to the traditional structure of diffuse interface models are necessary to improve their description of evaporation flows.

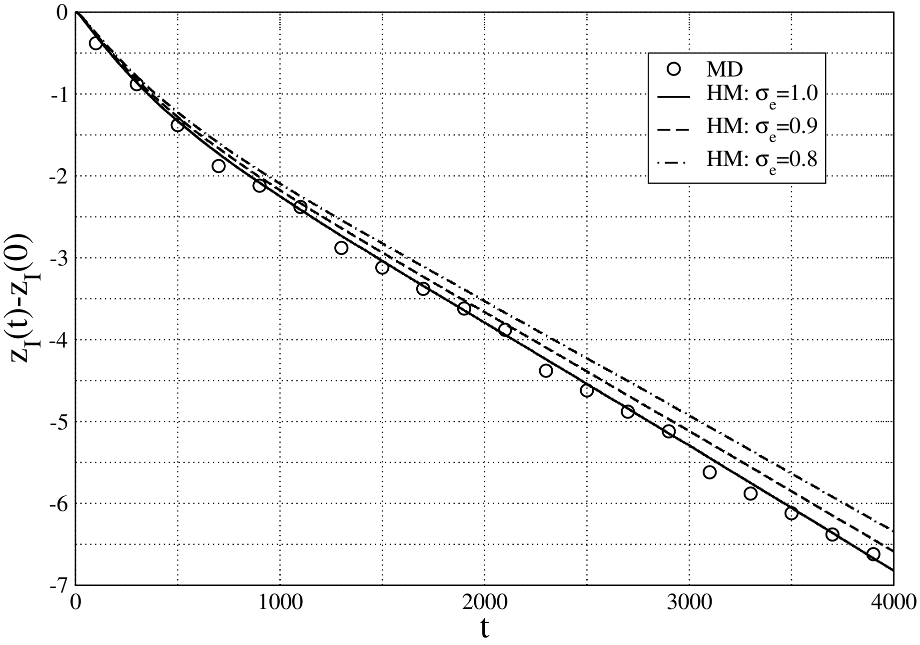

Figure 16: $T_l = 0.8$, $v_p = 0.2$. Effect of evaporation coefficient on interface recession. Diffuse re-emission of reflected vapor flux is assumed.

T	$K^{(d)}$	$\gamma^{(d)}$	$K^{(st)}$	$\gamma^{(MD)}$
0.8	3.4	0.54	4.1	0.60
0.9	3.8	0.39	3.75	0.38
1.0	3.7	0.21	4.1	0.23

Table A.4: Setting of Korteweg coefficient from density profiles or surface tension. $K^{(d)}$ is the value determined from the MD density profile, whereas $K^{(st)}$ is determined from the MD surface tension $\gamma^{(MD)}$ data from Ref. [35] ($r_c = 3.0\sigma$). $\gamma^{(d)}$ is the surface tension computed from $K^{(d)}$. All quantities expressed in LJ units: ϵ/k_B for T, ϵ/σ^2 for γ and $\sigma^2\epsilon/m$ for K

Appendix A. DIM Sensitivity Analysis

As discussed above, the DIM model formulation is based on a constant Korteweg coefficient K, whose values have been determined by matching the DIM equilibrium density profile with the corresponding MD one. More precisely, solutions of Eq. (9) are obtained as a function of K, whose desired value is found by minimizing the average distance from MD data in the reference frame in which the DIM and MD density profiles maximum slope positions coincide. The tolerance has been tuned in order to determine the first decimal digit of K, for a given MD profile.

The value of K can be also obtained from Eq. (10), by equating γ to the LJ surface tension. This second method is expected to give different estimations of K because the DIM static stress tensor $\mathbf{P}^{(s)}$ (see Eq. (7)) only provides a *local* approximation of the *non-local* exact expression [31]. The deviation is expected to be more significant when the fluid temperature T_l is well below the critical temperature T_c, but to reduces when T_l approaches T_c [31]. Table A.4 shows the values of K, denoted as $K^{(d)}$, determined from fitting the DIM density profiles to MD data for three temperatures. The corresponding surface tension values are denoted as $\gamma^{(d)}$ and differ from the MD values from Ref. [35] where surface tension values of the LJ fluid are given as a function of temperature for the same cutoff radius used in the present MD simulations. As expected the difference is stronger at $T = 0.8$. In order to fit MD values of the surface tension,

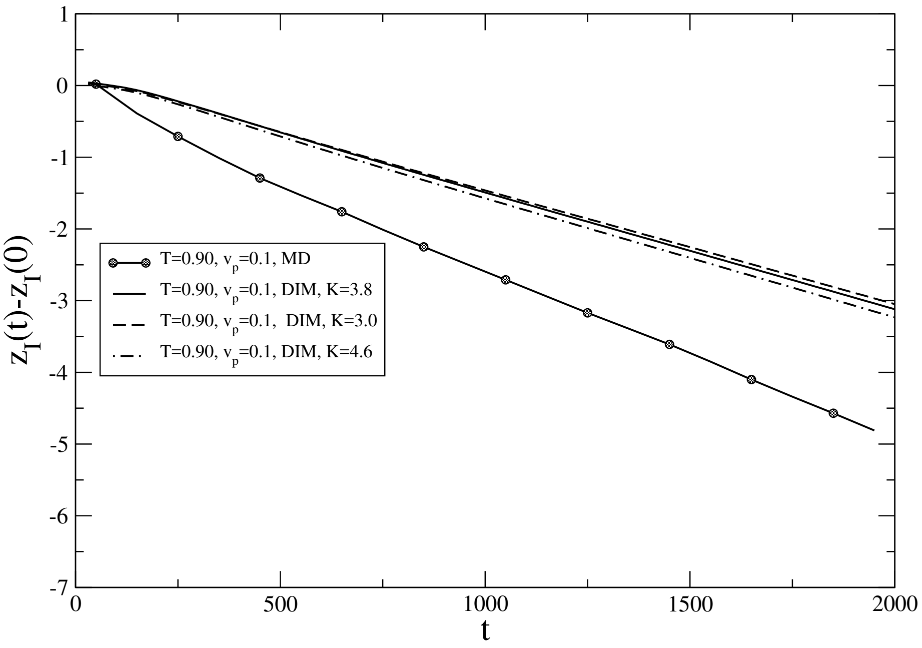

Figure A.17: $T_l = 0.9$, $v_p = 0.1$. Effect of global variation of the Korteweg coefficient K on DIM computed interface recession history. Initial slab thickness set to 64σ.

$\gamma^{(MD)}$, it is necessary to change the value of K from $K^{(d)}$ to $K^{(st)}$. As shown in Table A.4, the larger change (about 20%) occurs at $T = 0.8$. To investigate the sensitivity of DIM predictions to variations of K, a set of computations has been performed in correspondence of the values $K^{(d)}(1 \pm 0.2)$, *i.e.* prescribing a total variation of 40% centered on the nominal value. Figure A.17 shows the DIM results about the interface displacement in the case $T = 0.9$, $v_p = 0.1$, compared with the corresponding MD results. The evaporation rate exhibits low sensitivity to changes of K and changing the value of K from $K^{(d)}$ to $K^{(st)}$ does not improve the agreement with MD results. The sensitivity study has been extended to consider variations of K, μ and λ which are localized in the interface region. Accordingly, the following forms for the perturbed K and λ have been considered:

$$K' = K(T_l)\left(1 - C_K \left|\frac{\partial \rho}{\partial z}\right|\right) \tag{A.1}$$

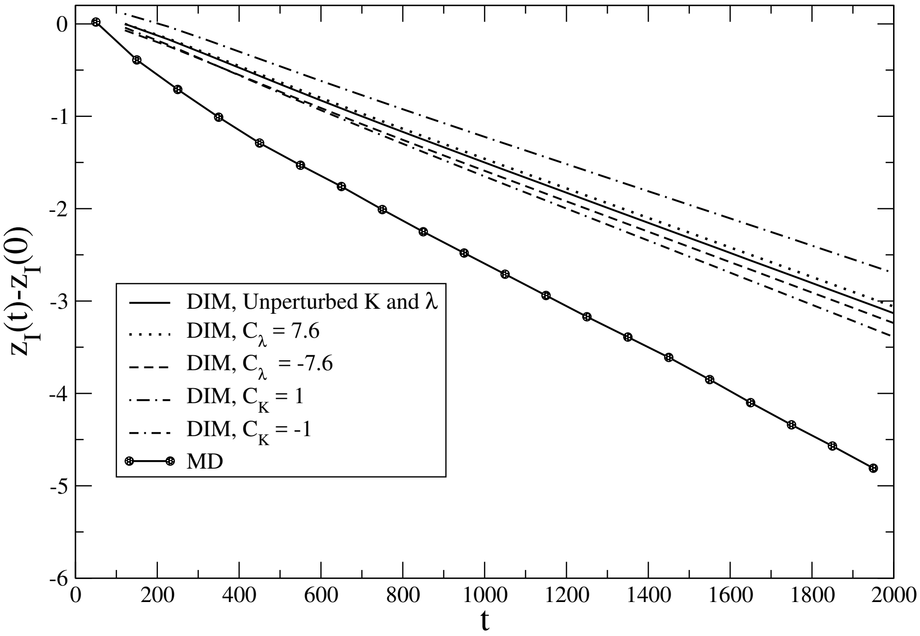

Figure A.18: $T_l = 0.9$, $v_p = 0.1$. Influence of changes in thermal conductivity and Korteweg coefficient K on DIM computed interface recession history.

$$\lambda' = \lambda(\rho, T)\left[1 - C_\lambda \left(\frac{\partial \rho}{\partial z}\right)^2\right] \tag{A.2}$$

which concentrate variations only in the interface region, where the density gradient is stronger. The viscosity can be also changed in the same way, however negligible effects on the flowfield have been observed and will not be reported here.

The constants C_K and C_λ have been varied to produce changes of the order 25% with respect to nominal values. It should be observed that the study had a purely exploratory character. Hence, the different dependence from the density gradient in Eqs. (A.1,A.2) is motivated by the need of obtaining a more or less sharp variation of the quantity to be varied in the interface, the particular choice being quite arbitrary. A representative case is shown in Figure A.18. As with the global variation of K described above, the considered local variations of DIM coefficients are not sufficient to change the slope of the interface displacement curves and improve the agreement with MD data.

[1] J. Dunn, J. Serrin, On the thermomechanics of interstitial working, Archive for Rational Mechanics and Analysis 88 (2) (1985) 95–133.

[2] D. M. Anderson, G. B. McFadden, A. A. Wheeler, Diffuse-Interface Methods in Fluid Mechanics, Annu. Rev. Fluid Mech. 30 (1998) 139–165.

[3] D. J. Korteweg, Sur la forme que prendent les équations du mouvements des fluides si l'on tien compte des forces capillaires causées par des variations de densité considérables mais continues et sur la théorie de la capillarité dans l'hypothèse d'une variation continue de la densité, Arch. Néerl. Sci. Exactes Nat. Ser. II 6 (1901) 1–24.

[4] A. Frezzotti, Boundary conditions at the vapor-liquid interface, Physics of Fluids 23 (3) (2011) 030609.

[5] S. Fujikawa, T. Yano, M. Watanabe, Vapor-Liquid Interfaces, Bubbles and Droplets: Fundamentals and Applications, Springer-Verlag, Heidelberg, 2011.

[6] B. Nadiga, S. Zalesky, Investigations of a two-phase fluid model, Eur. J. Mech.,B/Fluids 6 (1996) 885–896.

[7] A. Onuki, Dynamic van der waals theory, Physical Review E - Statistical, Nonlinear, and Soft Matter Physics 75 (3). `doi:10.1103/PhysRevE.75.036304`.

[8] F. Magaletti, L. Marino, C. Casciola, Shock wave formation in the collapse of a vapor nanobubble, Physical Review Letters 114 (6). `doi:10.1103/PhysRevLett.114.064501`.

[9] D. Bedeaux, E. Johannessen, A. Røsjorde, The nonequilibrium van der waals square gradient model. (i). the model and its numerical solution, Physica A 330 (2003) 329–353.

[10] V. Babin, R. Hoyst, Evaporation of a thin liquid film, J. Chem. Phys. 122 (2005) 024713.

[11] C. Cercignani, Rarefied Gas Dynamics: From Basic Concepts to Actual Calculations, Cambridge University Press, 2000.

[12] Y. Sone, Kinetic theoretical studies of the half-space problem of evaporation and condensation, TTSP 29 (3-5) (2000) 227–260.

[13] P. Barbante, A. Frezzotti, L. Gibelli, A comparison of molecular dynamics and diffuse interface model predictions of lennard-jones fluid evaporation, in: J. Fan (Ed.), Proceedings Of The 29th International Symposium On Rarefied Gas Dynamics, Vol. 1628 of AIP Conference Proceedings, American Institute of Physics, 2014, pp. 893–900. `doi:10.1063/1.4902688`.

[14] J. K. Johnson, J. A. Zollweg, K. E. Gubbins, The lennard-jones equation of state revisited, Molecular Physics 78 (3) (1993) 591–618.

[15] G. Galliero, C. Boned, A. Baylaucq, Molecular Dynamics Study of the Lennard-Jones Fluid Viscosity: Application to Real Fluids, Ind. Eng. Chem. Res. 44 (2005) 6963–6972.

[16] M. Bugel, G. Galliero, Thermal Conductivity of the Lennard-Jones Fluid: an Empirical Correlation, Chemical Physics 352 (2008) 249–257.

[17] C. Cercignani, The Boltzmann Equation and Its Applications, Springer-Verlag, Berlin, 1988.

[18] T. Ytrehus, Theory and experiments on gas kinetics in evaporation, in: J. L. Potter (Ed.), Rarefied gas dynamics: technical papers selected from the 10th International Symposium on Rarefied Gas Dynamics, Snowmass-at-Aspen, CO - July 1976, Vol. 51 of Progress in astronautics and aeronautics, American Institute of Aeronautics and Astronautics, 1977, p. 1197.

[19] T. Tsuruta, H. Tanaka, T. Masuoka, Condensation/evaporation coefficient and velocity distribution at liquid-vapor interface, Int. J. Heat and Mass Transf. 42 (1999) 4107–4116.

[20] R. Meland, A. Frezzotti, T. Ytrehus, B. Hafskjold, Nonequilibrium molecular-dynamics simulation of net evaporation and net condensation, and evaluation of the gas-kinetic boundary condition at the interphase, Physics of Fluids 16 (2004) 223–243.

[21] M. Allen, D. Tildesley, Computer Simulation of Liquids, Clarendon Press, 1989.

[22] J.-P. Hansen, I. McDonald, Theory of Simple Liquids, Academic Press, London, UK, 2006.

[23] S. Chapman, T. G. Cowling, The Mathematical Theory of Non-Uniform Gases, Cambridge University Press, Cambridge UK, 1990.

[24] P. D. Neufeld, A. R. Janzen, R. A. Aziz, Empirical equations to calculate 16 of the transport collision integrals $\Omega(l,s)$ for the Lennard-Jones $(12-6)$ potential, Journal of Chemical Physics 57 (3) (1972) 1100–1102.

[25] A. Frezzotti, A numerical investigation of the steady evaporation of a polyatomic gas, European Journal of Mechanics - B/Fluids 26 (1) (2007) 93–104.

[26] H. Bijl, P. Wesseling, A Unified Method for Computing Incompressible and Compressible Flows in Boundary-Fitted Coordinates, J. of Comput. Phys. 141 (1998) 153–173.

[27] J. Ferziger, M. Peric, Computational Methods for Fluid Dynamics, 3rd Edition, Springer, 2002.

[28] C. Hirsch, Numerical Computation of Internal and External Flows, 2nd Edition, Vol. 1, Elsevier, 2007.

[29] N. P. Waterson, H. Deconinck, Design Principles for Bounded Higher-order Convection Schemes a Unified Approach, J. of Comput. Phys. 224 (2007) 182–207.

[30] S. Gottlieb, C. W. Shu, Total Variation Diminishing Runge-Kutta Schemes, Mathematics of Computation 67 (1998) 73–85.

[31] A. Frezzotti, L. Gibelli, S. Lorenzani, Mean field kinetic theory description of evaporation of a fluid into vacuum, Phys. Fluids 17 (2005) 012102.

[32] Y. Tang, First-order mean-spherical approximation for interfacial phenomena: a unified method from bulk-phase equilibria study, J. of Chem. Physics 123 (2005) 204704.

[33] A. Frezzotti, Kinetic theory description of the evaporation of multi-component substances, in: C. Shen (Ed.), Rarefied Gas Dynamics, Proceedings of the 20th International Symposium, 19-23 August 1996, Beijing, China, Peking University Press, Beijing, China, 1997, pp. 837–846.

[34] G. A. Bird, Molecular Gas Dynamics and the Direct Simulation of Gas Flows, Clarendon Press, Oxford, 1994.

[35] P. Grosfils, J. F. Lutsko, Dependence of the liquid-vapor surface tension on the range of interaction: A test of the law of corresponding states, Journal Of Chemical Physics 130 (2009) 054703.